Characteristics of laminar ion beams accelerated via a few-joule laser pulse

Toshimasa Morita

Quantum Beam Science Research Directorate, National Institutes for Quantum Science and Technology, 8-1-7 Umemidai, Kizugawa-shi, Kyoto 619-0215, Japan

(Received 20 May 2022; accepted 14 September 2022; published 10 October 2022)

Laser-driven carbon ion beams from a carbon foil target via a 2.5-J laser pulse are investigated with three-dimensional particle-in-cell simulations. An ion bunch with a narrow energy range exhibits a thin shell shape with a certain diameter. The ion cloud has a layered structure of these ion bunches with different energies. The divergences of the ion bunch in the laser inclination direction and perpendicular to it are different in an oblique incidence laser. In addition, theoretical formulas for the radius of the generated ion beam and the energy spectrum are derived, and they are shown to be in good agreement with the simulation results.

DOI: 10.1103/PhysRevResearch.4.043020

I. INTRODUCTION

The recent progress in compact laser systems has been significant. Laser ion acceleration is a compelling application of high-power compact lasers [1,2]. If a compact laser system can generate ions with sufficiently high energy and quality, low-cost compact accelerators would become feasible. However, the ion energies that have been currently achieved by laser ion acceleration are insufficient for applications such as particle therapy [3,4]. Therefore, there are two ways for the study of the laser ion acceleration to proceed: (i) evaluating the conditions required to produce higher-energy ions (including high-power laser development) [5–14] and (ii) an investigation aimed at practical application using the currently available ion energies.

In the former, the focus is on the maximum energy of the obtained ions. In general, the higher the energy of ions, the smaller their number. Therefore, the number of ions in an ion bunch, with a narrow energy width, containing the maximum-energy ions is very small. However, numerous applications require an ion beam with a sufficient number of ions [15,16]. Therefore, in this way, it is necessary to satisfy the two conflicting requirements. In this study, we take the latter way, and it is assumed that a widely commercially available laser is used. We focused not only on the maximum energy of the generated ions but also on the lower-energy ions, because they are produced in large quantities [17]. Our aim is to find a reasonable method to generate a large number of not-so-high-energy ions (several MeV/u) within a narrow solid angle and to clarify the characteristics of these ion beams. Such an ion beam can be applied, as an injector in heavy-ion radiotherapy facilities.

By using laser acceleration injectors, it is possible to reduce the size and price of radiotherapy facilities [18]. The energy of the carbon ions produced by current injectors is 4 MeV/u, and the same energy is required for laser acceleration injectors. In addition, because the beam capture diameter in the subsequent device is several cm wide, the ions within a narrow solid angle (several msr) will be utilized.

In this study, a foil is used as the target because of its ease of preparation and handling. Currently, carbon ions are most commonly used in heavy-ion radiotherapy. Therefore, a carbon foil target is selected. Widely commercially available laser conditions, i.e., a relatively low laser energy and not extremely small spot size and pulse duration, are considered. This is because the laser used in a compact accelerator will inevitably have widely commercially available performance due to the requirements for a smaller size and lower price of the accelerator.

The remainder of this paper is organized as follows: In Sec. II, the simulation parameters are presented. Section III presents the characteristics of the accelerated carbon ions. The analytical considerations are presented in Sec. IV. Section V presents the properties of the generated carbon ion beams at an energy of around 4 MeV/u. Section VI summarizes the main results of this study.

II. SIMULATION MODEL

Simulations were performed using a three-dimensional (3D) parallelized electromagnetic code, based on the particle-in-cell (PIC) method [19], which was developed, has been improved and used by our institute to simulate laser plasma interactions [11–13,20,21]. The parameters used in the simulations are as follows.

An idealized model is used in which a Gaussian p-polarized laser pulse is obliquely incident, 45°, on a foil target represented by a collisionless plasma. The laser pulse energy is 2.5 J and focused to a spot size of 5 μm full width at half maximum (FWHM), and the pulse duration is 50 fs (FWHM). Corresponding to the laser pulse with peak intensity, I, is

1.7×10^{20} W/cm^2, the peak power is 47 TW, and dimensionless amplitude $a_0 = q_e E/m_e \omega c = 9$. The laser wavelength is $\lambda = 0.8$ μm.

A foil target consisting of carbon is used in this study. It has been reported that high-energy ions are generated at 0.1 μm foil thickness when an 18-J laser pulse is irradiated onto a polyethylene (CH_2) foil target [13]. Because the energy of the laser pulse used in this study is much lower than that of the aforementioned laser pulse, and moreover, the electron density in the fully striped carbon target is about two times that of CH_2, the foil thickness at which the maximum energy occurs is considered to be much thinner than 0.1 μm. However, it is difficult to achieve extremely thin thicknesses. Therefore, the foil thickness, ℓ_t, is set to 1 μm as the thinnest thickness considered feasible.

The ionization state of the carbon ion is assumed to be $Z_i = +6$. The electron density is $n_e = 6 \times 10^{23}$ cm^{-3}, i.e., $n_e = 345 n_{\rm cr}$, where $n_{\rm cr}$ denotes the critical density. The total number of quasiparticles is 2×10^{11}. A triangular particle shape, i.e., first-order weighting, is used.

The number of grid cells is $4000 \times 3456 \times 2500$ along the X, Y, and Z axes. Correspondingly, the simulation box size is $72 \times 62 \times 45$ μm. The boundary conditions for the particles and fields are periodic in the transverse (Y, Z) directions and absorbing at the boundaries of the computation box along the X axis. We set the electric field of the laser pulse to be along the XY plane so that the magnetic field of the laser pulse is along the Z axis. The laser-irradiated side of the foil surface is placed at $X = 36$ μm, and the center of the laser pulse is located 13 μm in front of its surface in the X direction and 13 μm above the foil center in the Y direction. The laser propagation direction is 45° downward, i.e., the direction vector is $(1, -1, 0)$. An xyz-coordinates system is used throughout the text and figures. The origin of the coordinate system is located at the center of the laser-irradiated surface of the initial target, and the directions of the x, y, and z axes are the same as those of the X, Y, and Z axes, respectively. Therefore, the x axis denotes the direction perpendicular to the target surface, and the y and z axes lie in the target surface.

III. ACCELERATED CARBON IONS

In this section, we present the simulation results. The ion acceleration scheme changes with variations in the laser intensity I and/or target thickness ℓ_t (areal density of electrons $n_e \ell_t$ to be exact). Therefore, the acceleration scheme can be determined using the value of $I/n_e \ell_t$. Under our conditions, because $I/n_e \ell_t = 3$ W/electron, which is considerably less than $I/n_e \ell_t > 500$ W/electron which is a condition that would be nonhomeomorphic acceleration [20] (radiation pressure acceleration), and therefore the ion acceleration scheme is the Coulomb explosion.

Figure 1 shows the particle distribution and electric field magnitude at times $t = -63, 3, 70$, and 203 fs. Half of the electric field box has been excluded to reveal the internal structure in Fig. 1(a), and their cross sections in the xy plane are shown in Fig. 1(b). Carbon ions are classified by color in terms of their energy. It is assumed that $t = 0$ when the center of the laser pulse, where I is the strongest, reaches the laser-irradiated surface of the initial target. That is, more

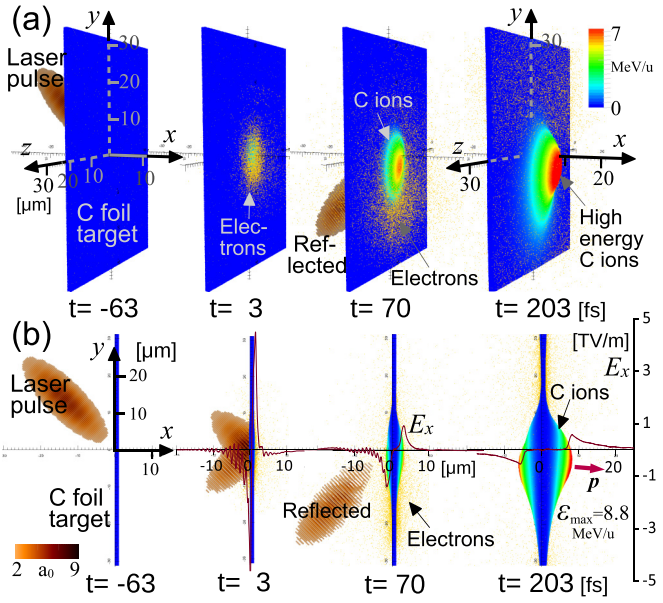

FIG. 1. (a) Laser pulse is oblique incident, 45°, on carbon foil target. A 3D view is given of the particle distribution and electric field magnitude (isosurface for value $a_0 = 2$) at each time. Half of the electric field box has been excluded to reveal the internal structure. The carbon ions color corresponds to their energy. (b) A 2D projection is shown as viewed along the z axis. Here half of the ion cloud also has been excluded. The red thick arrow shows the momentum vector, $\boldsymbol{p}$, of the high-energy carbon ions. The x component of the electric field, $E_x(x)$, on the x axis are shown by solid lines.

than half of the laser pulse does not interact with the target when $t < 0$, and more than half of the interaction is complete at $t \geqslant 0$. The simulation start time is $t = -63$ fs. The initial shapes of the laser pulse and target are shown at $t = -63$ fs. The laser pulse is defined on the $-x$ side of the target and travels diagonally toward the $+x$ side. At $t = 3$ fs, the laser pulse undergoes strong interactions with the target. About half of the laser pulse has interacted with the target, whereas the other half does not. A portion of the laser pulse is reflected from the target. Subsequently, the carbon ion cloud explodes by Coulomb explosion and grows over time. High-energy carbon ions are distributed at the $+x$ side tip of the ion cloud and shifted slightly in the $-y$ direction.

At $t = 70$ fs, the interaction between the laser pulse and target ended, and the reflected laser pulse is moving in the $-x$ direction (diagonally downward). The target is slightly expanded. In the electron distribution, the electrons that are pushed out from the target are distributed in large numbers in the $-y$ region [21]. At $t = 203$ fs, the target is largely expanded, with high-energy areas occurring at each tip of the ion cloud on the $+x$ and $-x$ sides. The maximum energy of the carbon ions is 8.8 MeV/u and occurs at the tip of the $+x$ side of the ion cloud. The dark-red arrow represents the momentum vector of the high-energy carbon ions. This momentum vector is slightly tilted downward, in the $-y$ direction [11,21,22], and its angle with the x axis is $-5°$. Although it is lower than that of the $+x$ side, relatively high-energy ions are also generated at the tip of the ion cloud on the $-x$ side, with a maximum energy of 7.1 MeV/u. These ions travel in the

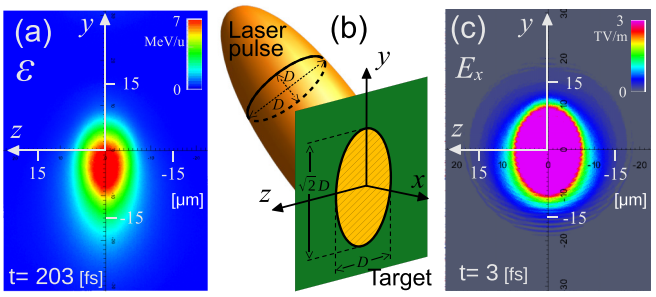

FIG. 2. (a) Carbon ion distribution at $t = 203$ fs. A 2D projection of Fig. 1(a) is shown as viewed along the x axis. The high-energy ions are distributed in a vertically long elliptical shape. (b) Illustration of the laser pulse and target. The cross section of the laser pulse is a circle, but the distribution of the laser on the target is a vertically long ellipse. (c) E_x distribution on the target at $t = 3$ fs. E_x has a vertically long elliptical distribution. The purple area is more than 3 TV/m.

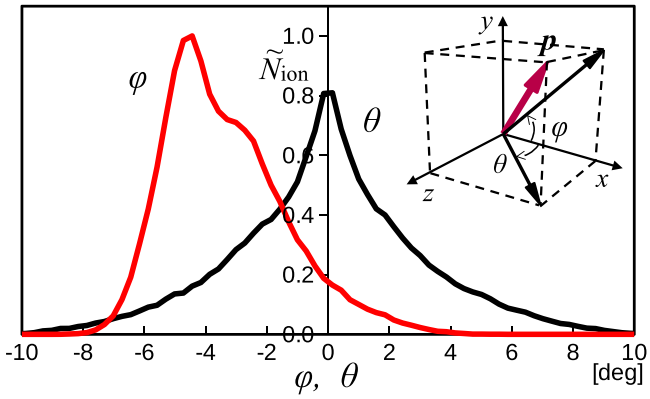

FIG. 3. Angular distribution of φ and θ of the ions of 3.8 MeV/u or more traveling in the $+x$ direction at $t = 203$ fs. It is normalized by the maximum value of φ, $\tilde{N}_{\rm ion} = N_{\rm ion}/N_{\rm ion,max}$. The momentum vector of an ion is tilted downward ($-y$ direction) on average but not horizontally. The horizontal spread of the momentum vector is wider than the vertical direction. Inset: The momentum vector of an ion, φ, and θ.

opposite direction to the ions on the $+x$ side, i.e., in the $-x$ direction. High-energy ions also appear on the $-x$ side because the acceleration scheme in this study is the Coulomb explosion of the target. The distribution of E_x on the x axis is shown as a solid line. The ions are accelerated by E_x. The largest E_x in the figures occurs on the $+x$ side surface of the target at $t = 3$ fs, which is 5 TV/m. At this time, a similarly large E_x also occurs on the $-x$ side surface in the opposite direction. Therefore, it can be said that ion acceleration mainly occurs at around $t = 3$ fs when the laser and target interact strongly. Subsequently, E_x is remarkably small and decreases over time. At $t = 203$ fs, it is observed that the E_x inside the ion cloud is approximately 0.

The accelerating electric field $E_\parallel$ (electric field in the direction of ion motion) experienced by the maximum-energy ions is not equal to the E_x shown in Fig. 1(b). However, both the position of the ion and its direction of motion only marginally deviate from the x axis. Hence, $E_\parallel \sim E_x$. $E_\parallel/E_x$ (ratio of their maximum values) at $t = 3$ fs, when the strongest acceleration occurs in the figure, and at the final time $t = 203$ fs are 1.04 and 0.98, respectively. The change in total energy at times up to ∼70 fs (the time when neither the electromagnetic fields nor particles go out through the x boundaries) is less than 1%. Thus, energy is conserved in the simulation. The maximum/mean ion energies normalized by the value of the final time $t = 203$ fs are 3.5, 1.1, 1.0, and 1.0 at $t = 3$, 70, 137, and 203 fs, respectively. This ratio has converged to a steady-state value. Hence, at the time when the laser and target are interacting ($t = 3$ fs), the maximum-energy ions are selectively accelerated more strongly than other ions, compared with other times. This degree of selectivity decreases as the laser and target interaction comes to an end and almost does not change for $t \geqslant 70$ fs. At normal incidence, the maximum-energy ions appear on the x axis and is not tilted in the y direction, and its maximum energy is lower than that at 45° incidence [11].

In the following, we consider the characteristics of the generated ion cloud. First, the spatial distribution of the ion cloud is considered. Figure 2(a) shows a 2D view of the ion distribution at $t = 203$ fs in Fig. 1(a), as viewed along the x axis. The high-energy ions are distributed in a long elliptical shape in the y direction, and its center is shifted toward the $-y$ direction.

Hereinafter, we refer to the y axis direction as the vertical and the z axis direction as the horizontal. The generated ion distribution is a vertically long ellipse because the laser is an oblique incidence inclined in the y direction. In our simulation, the cross section of the laser pulse is circular, but its shape on the target surface is elliptical because of oblique incidence [see Fig. 2(b)]. Consequently, the distribution of the acceleration field generated on the target also becomes elliptical [Fig. 2(c)]. Figure 2(c) shows the distribution of the x direction electric field (accelerating field), E_x, on the $+x$ side surface of the target at $t = 3$ fs, which is the time when the strongest E_x occurs. Because ions are produced from this elliptically distributed acceleration field, their distribution becomes elliptical. From the details shown in Fig. 2(c), it can be seen that the accelerating electric field is egg shaped. That is, the left and right sides are symmetrical with respect to the y axis, but the top and bottom sides are not symmetrical with respect to the z axis, and they are distributed horizontally longer in the region where $y < 0$ than in the region where $y > 0$. In addition, from the y coordinate values of the light blue area, it is clear that this area is distributed farther in the $-y$ direction than in the $+y$ direction. This is because the laser is obliquely incident; thus, more electrons are distributed in the area of $y < 0$ outside the target (see $t = 70$ fs in Fig. 1). The accelerated ions generated from this elliptical region at $t = 3$ fs are thereafter more shifted toward the $-y$ direction due to the effect of the electron distribution [21].

Next, the traveling direction of the generated ions, i.e., the direction of their momentum vectors, is considered. Figure 3 shows the angular distribution of the angle between the momentum vector of an ion of 3.8 MeV/u or more that is accelerating toward $+x$ side and the x axis at $t = 203$ fs. Energies of 3.8 MeV/u or more are selected because we are focusing on carbon ions at around 4 MeV/u (to be discussed

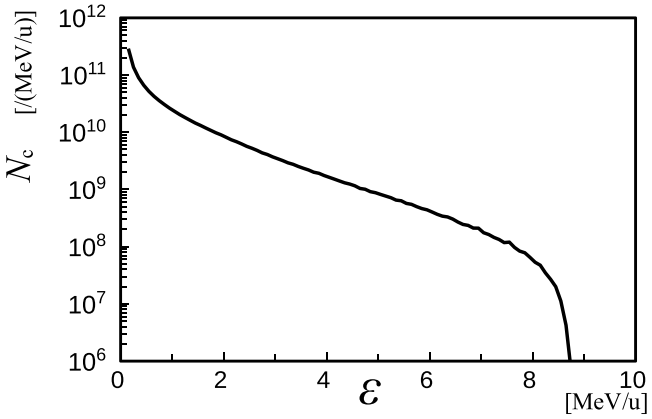

FIG. 4. Energy spectrum of the carbon ions traveling in the $+x$ direction obtained in the simulation at $t = 203$ fs. It is a monotonically decreasing.

in detail in Sec. V). φ is the angle between the momentum vector projected onto the xy plane and the x axis, i.e., the vertical tilt, and θ is the angle when projected onto the xz plane, i.e., the horizontal tilt (see the inset). Modes are $\varphi_{\rm mode} = -4.4^\circ$ and $\theta_{\rm mode} = 0^\circ$, that is, the traveling directions of these ions are, on average, slightly tilted in the $-y$ direction, vertical direction, but not in the z direction, horizontal direction. The vertical direction, φ, is distributed in the range from -8° to 4°, and the horizontal direction, θ, is distributed approximately in the range from -10° to 10°. Their widths are $\Delta\varphi = 12^\circ$ and $\Delta\theta = 20^\circ$, respectively, i.e., the horizontal spread (variance of the distribution) of the velocity vector is wider than the vertical direction. That is, the ion cloud is expanding more in the horizontal direction.

Figure 4 shows the energy spectrum of carbon ions accelerated in the $+x$ direction at $t = 203$ fs. Carbon ions are generated on both the $+x$ and $-x$ sides of the target, but here it is assumed that the ions are received and used by some device installed behind the target, i.e., in the $+x$ direction. Therefore, only the ions that traveled to the $+x$ side are considered. The vertical axis is provided in units of the number of carbon ions per 1 MeV/u width. The horizontal axis represents the energy of the carbon ion $\mathcal{E}$. The number of ions produced decreases with increasing energy. Therefore, if a large number of accelerated ions are needed, then ions in the lower-energy range should be used, not near the maximum energy. This is the reason for our focus on ions in the low-energy region. At 8 MeV/u, which is near the maximum energy, there are 6×10^7 /(MeV/u) ions, but at 4 MeV/u, which is half the maximum energy, there are 2×10^9 /(MeV/u) ions, which is about 30 times the number of ions. The number of ions with a 10% energy range (3.8–4.2 MeV/u) at 4 MeV/u is approximately 7×10^8, which is sufficient for some applications (e.g., particle therapy). In Sec. V, the ions generated in this energy range are discussed in detail.

In our simulation, because the acceleration scheme is a Coulomb explosion due to the low laser intensity and the intensity distribution is Gaussian, the energy spectrum monotonically decreases. The next section discusses this issue in more detail.

IV. ANALYTICAL CONSIDERATION

We consider the Coulomb explosion regime, i.e., TNSA [23], as the acceleration scheme with a thin foil compared to the spot size, similarly to that shown above. In this case, the maximum ion energy is generated from the opposite side surface of the laser irradiation surface of the target, and from there, the generated ion energy decreases with depth toward the inside of the target, and near the center of the target thickness, the ion energy is approximately zero. In the region from there to the laser-irradiated surface, the ion is accelerated in the opposite direction, $-x$ direction, and the ion energy increases again to the laser-irradiated surface.

In this study, we focus on ions accelerated to the $+x$ side. Therefore, we consider the area from near the center of the target thickness to the target surface on the opposite side of the laser-irradiated surface. In this section, this surface will be simply described as the target surface.

A. Ion bunch radius

The intensity, I, distribution of the laser pulse is Gaussian in the direction perpendicular to the laser traveling direction in our simulation. Therefore, when the origin is at the position on the target surface where the laser center is located, the laser electric field in any direction on the target surface from the origin is a Gaussian distribution. That is, at a certain time, the laser electric field at the r position on the surface of the target is given by

$$E_l(r) = E_l(0)e^{-ar^2}, \tag{1}$$

where E_l is the amplitude of the electric field, $|\boldsymbol{E}_l|$; $E_l(0)$ is its value at the origin, i.e., at the laser pulse center; and "a" is the coefficient that defines the shape of the Gaussian distribution, which is determined from the distribution shape of the laser intensity, I.

It is considered that the larger the laser electric field, the larger the accelerating field generated on the target by laser irradiation. Then, we assume that the accelerating electric field $E_s(r)$ generated at position r on the target surface by laser irradiation in the direction perpendicular to the surface is proportional to the laser electric field $E_l(r)$ at that position. That is, it is assumed that $E_l(r) = k_e E_s(r)$, where k_e is a proportional constant. By substituting this into Eq. (1), we obtain the following relational equation for the accelerating electric field on the target surface:

$$E_s(r) = E_s(0)e^{-ar^2}. \tag{2}$$

Let $\mathcal{E}(r)$ be the maximum ion energy generated from the r position and $I(r)$ be the laser intensity at that position. It was shown that when the accelerating process is a Coulomb explosion of the target, i.e., TNSA, the maximum ion energy, $\mathcal{E}_{\rm max}$, is proportional to the square root of the maximum laser intensity, $\sqrt{I_{\rm max}}$ [20]. Here $\mathcal{E}_{\rm max}$ is generated from the origin, i.e., $\mathcal{E}_{\rm max} = \mathcal{E}(0)$, and $\sqrt{I_{\rm max}}$ is also the value at the origin, i.e., $\sqrt{I_{\rm max}} = \sqrt{I(0)}$. That is, there is an $\mathcal{E}(0) \propto \sqrt{I(0)}$ relationship. Generalizing this, we assume here that the maximum ion energy, $\mathcal{E}(r)$, generated from position r is proportional to the square of the laser intensity at that position, $\sqrt{I(r)}$, i.e., $\mathcal{E}(r) \propto \sqrt{I(r)}$. Then, from the relation

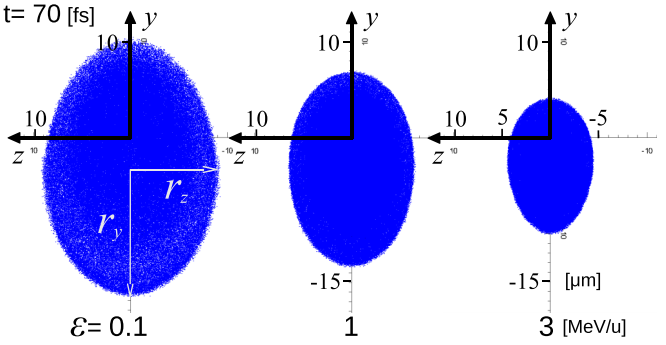

FIG. 5. Two-dimensional projections of ion bunches with energies of 0.1, 1, and 3 MeV/u at $t = 70$ fs are shown as viewed along the x axis. The ion energy range for each bunch is ±5%. Vertical radius, r_y, and horizontal radius, r_z, are shown. Ion bunches have a vertically long shape. The higher the energy, the smaller the radii.

$\sqrt{I(r)} \propto E_l(r) \propto E_s(r)$, we obtain

$$E_s(r) = k_\epsilon \mathcal{E}(r), \tag{3}$$

where k_ϵ is a proportionality constant. By substituting this into Eq. (2), we obtain $\mathcal{E}(r) = \mathcal{E}(0)e^{-ar^2}$. Solving this with r and rewriting $\mathcal{E}(0)$ as $\mathcal{E}_{\max}$, we obtain

$$r = \sqrt{-\frac{1}{a}\log\frac{\mathcal{E}(r)}{\mathcal{E}_{\max}}}, \tag{4}$$

where r indicates the distance from the origin to the position where the maximum energy of the generated ion is $\mathcal{E}(r)$. When a certain amount of energy, $\mathcal{E}$, is provided, r is determined by substituting $\mathcal{E}(r)$ with $\mathcal{E}$ in Eq. (4). From the area within this r, ions with energy higher than $\mathcal{E}$ are produced and $\mathcal{E}$ ions are also produced. However, farther than r, no ions with energy greater than $\mathcal{E}$ occur. Thus, r is the maximum distance from the origin to the position where ions of energy $\mathcal{E}$ occur. In other words, the radius of the ion bunch with energy $\mathcal{E}$ is given by r.

Figure 5 shows a 2D view of the ion bunches with energies of 0.1, 1.0, and 3.0 MeV/u, as viewed along the x axis, immediately after the interaction between the laser pulse and the target ends ($t = 70$ fs). Here the ion energy range is ±5%, that is, a 0.1 MeV/u ion is an ion with energy in the range of 0.095–0.105 MeV/u and the same for other energies. The distances from the center to the edge of the ion bunch in the y and z directions are defined as the vertical radius $= r_y$ and horizontal radius $= r_z$, respectively (see Fig. 5). Because the laser is obliquely incident, the ion bunch has a long vertical distribution, $r_y > r_z$. The radii r_y and r_z are smaller for higher-energy ion bunches. The distribution of the 4 MeV/u ion bunch will be shown in detail later (in Sec. V), and the ion bunches shown here are similar to that, i.e., the thickness is thin and shaped like a shell. The outlines of each ion bunch are clear and are not distributed in such a way that there are no boundaries as the number of ions gradually becomes increasingly sparser.

Although the geometry of the ion bunches at only three energies has been shown, more energies, $\mathcal{E}$, and radii, r, are shown in Fig. 6. The results of the simulation and theoretical formula in Eq. (4) are shown. In this study, the Gaussian

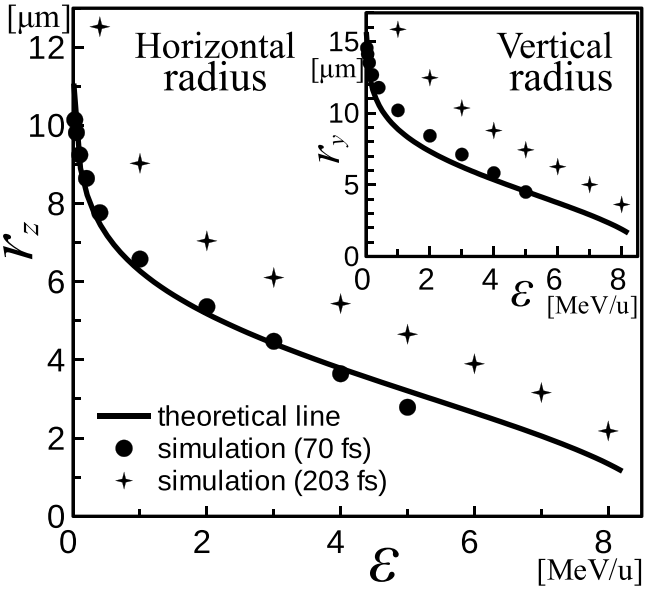

FIG. 6. Simulation and theoretical results of horizontal radius, r_z, of carbon ion bunch at each energy. Inset: Their vertical radius, r_y.

distribution shapes in the vertical and horizontal directions are different, i.e., "a" is different, because of the oblique incidence; thus results are shown for each direction. The theoretical and simulation results of r are in good agreement in both the vertical and horizontal directions at $t = 70$ fs, immediately after the laser and target interaction ended. This good agreement indicates that the two assumptions in the derivation of the r equation are correct. $t = 203$ fs, the Coulomb repulsion between ions in the ion cloud causes the ion bunch to expand; consequently, the simulation results are larger than the theoretical results.

In above consideration, we showed the case where the distribution of I is Gaussian. On generalizing Eq. (1), when it is given by $E_l(r) = E_l(0)f(r)$, using the function $f(r)$ for the distribution shape, Eq. (4) becomes $r = f^{-1}[\mathcal{E}(r)/\mathcal{E}(0)]$, where $f(r)$ is assumed to be normalized to $f(0) = 1$.

B. Energy spectrum

Next, a theoretical study on the number of generated ions is present. For simplicity, we consider the normal incidence of the laser.

First, we determine the volume of the region in the initial target that will become ions in the energy range from $\mathcal{E}_1$ to $\mathcal{E}_1+\Delta\mathcal{E}$. Let r_1 be the position on the target surface where an ion with $\mathcal{E}_1$ energy appears from the surface. That is, for $r > r_1$, $\mathcal{E}(r) < \mathcal{E}_1$ and ions of $\mathcal{E}_1$ energy do not occur.

At a certain position r on the target surface, where $r < r_1$, the thickness direction, i.e., the depth direction, of the target is considered. The origin is placed at the center of the target thickness, and the axis is taken from this point toward the target surface. We consider an electric field, i.e., an accelerating field, oriented in the direction of this axis. It is assumed that the electric field is zero at the origin, and it at each position from there to the surface changes linearly to the surface electric field, $E_s(r)$. At r, the ions of the energy range from $\mathcal{E}_1$ to $\mathcal{E}_1+\Delta\mathcal{E}$ are generated inside the target. Let E_1 be the

electric field at the position where the ions that become the energy of $\mathcal{E}_1$ are located, $E_1+\Delta E$ be the electric field at the position where the ions that become the energy of $\mathcal{E}_1+\Delta\mathcal{E}$ are located, and the distance between them be $\delta_1(r)$. That is, we assume that the ions of the range $\mathcal{E}_1$ to $\mathcal{E}_1+\Delta\mathcal{E}$ occur from the position where the electric field is in the range E_1 to $E_1+\Delta E$. At this time, there exist a relationship $E_s(r)/\ell = \Delta E/\delta_1(r)$. Therefore,

$$\delta_1(r) = \frac{\ell\Delta E}{E_s(r)}, \tag{5}$$

where ℓ is the distance from the origin to the target surface; here, half of the target thickness, $\ell_t/2$, is considered.

Next, let the position on the target surface where the laser center is located be the origin, and consider polar coordinates on the surface, let r be the distance from the origin and θ be the angle from the horizontal axis. At position (r, θ), the small area $\Delta A = r\Delta\theta\Delta r$ where the bound is the small length Δr and small angle $\Delta\theta$. At this position, thickness $\delta_1(r)$, which becomes the energy ranging from $\mathcal{E}_1$ to $\mathcal{E}_1+\Delta\mathcal{E}$, is determined by Eq. (5); thus, its volume is $\Delta V = \Delta A\delta_1(r) = r\Delta\theta\Delta r\ell\Delta E/E_s(r)$. Consequently, the total volume, V, of the region that becomes the energy in the range of $\mathcal{E}_1$ to $\mathcal{E}_1+\Delta\mathcal{E}$ is obtained by integrating ΔV with the target region, V_1, in $r \leqslant r_1$, i.e., integrating θ with $0-2\pi$ and r with $0-r_1$,

$$\begin{aligned} V &= \int_{V_1}\Delta V = \int_0^{r_1}\int_0^{2\pi}\frac{\ell\Delta E}{E_s(r)}rd\theta dr \\ &= 2\pi\ell\Delta E\int_0^{r_1}\frac{r}{E_s(r)}dr. \end{aligned}$$

Substituting Eq. (2) into the above equation, we obtain

$$\begin{aligned} V &= \frac{2\pi\ell\Delta E}{E_s(0)}\int_0^{r_1} re^{ar^2}dr = \frac{\pi\ell\Delta E}{aE_s(0)}(e^{ar_1{}^2}-1) \\ &= \frac{\pi\ell\Delta E}{a}\left[\frac{1}{E_s(r_1)}-\frac{1}{E_s(0)}\right]. \end{aligned} \tag{6}$$

Here the relationship $e^{ar_1{}^2} = E_s(0)/E_s(r_1)$ obtained from Eq. (2) is used. When the number density of the ions in the target is n_0, the number of ions at an energy range of $\mathcal{E}_1$ to $\mathcal{E}_1+\Delta\mathcal{E}$ is n_0V. This is expressed as $N(\mathcal{E}_1)\Delta\mathcal{E}$ using the number of ions per unit energy range, $N(\mathcal{E})$. Therefore, $N(\mathcal{E}_1)\Delta\mathcal{E} = n_0V$. Substituting Eq. (6) for V in this equation, and thereafter substituting the relations $\Delta E = k_\epsilon\Delta\mathcal{E}$, $E_s(r_1) = k_\epsilon\mathcal{E}(r_1) = k_\epsilon\mathcal{E}_1$, and $E_s(0) = k_\epsilon\mathcal{E}(0) = k_\epsilon\mathcal{E}_{\max}$ obtained from Eq. (3), we obtain

$$N(\mathcal{E}) = \frac{n_0\pi\ell}{a}\left(\frac{1}{\mathcal{E}}-\frac{1}{\mathcal{E}_{\max}}\right), \tag{7}$$

for the energy spectrum. Here $\mathcal{E}_1$ is rewritten as $\mathcal{E}$ in general notation.

If the target thickness, ℓ_t, is sufficiently thin relative to the laser intensity, then $\ell = \ell_t/2$ can be considered. However, in our simulation, ℓ_t is thick with 1 μm; thus, if $\ell = \ell_t/2$, then the results would be large, because relatively high-energy ions would be produced even from near a depth of 0.5 μm from the surface. That is, in a relatively thick target, the position where the electric field on the target surface decreases to zero is not at the thickness center position of the target, but closer to the surface, and ℓ needs to be its value.

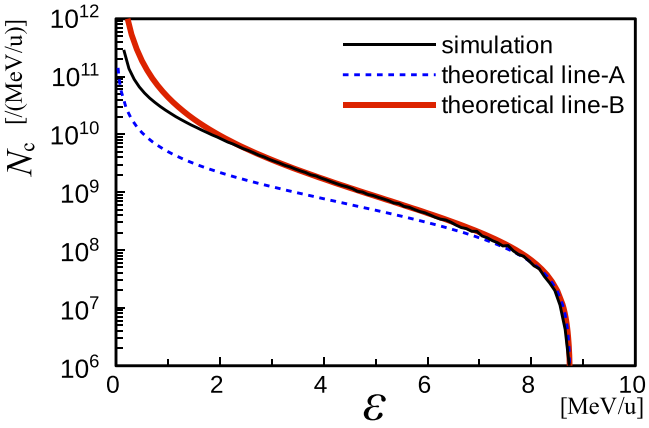

FIG. 7. Energy spectrum in theory and simulation. The dotted and red solid curves are given from Eqs. (7) and (8), respectively.

Figure 7 (line A) is the result for a value of ℓ of 1 nm. That is, the part from the target surface to a depth of 1 nm will be accelerated. The black solid line is the simulation result and is the same as shown in Fig. 4. The theoretical and the simulation results agree well in the high-energy range, $\mathcal{E} \gtrsim 7$ MeV/u.

Rewriting Eq. (5) in terms of the ion energy using the relationship in Eq. (3), we obtain $\delta_1(r) = \ell\Delta\mathcal{E}/\mathcal{E}(r)$. This implies that regardless of the energy of interest, if the energy range, $\Delta\mathcal{E}$, is the same, then the width of the region where ions of that energy occur is also the same. This is because we assumed that the generated ion energy, the accelerating electric field, in the target depth direction decreases linearly with depth. In contrast, assume that the generating ion energy decreases exponentially with ξ (i.e., the accelerating electric field decreases exponentially) as $\mathcal{E}(r)e^{-\xi\mathcal{E}(r)/\mathcal{E}_{\max}\ell}$, where ξ is the distance from the target surface; then the region width is $\delta_1(r)\mathcal{E}_{\max}/\mathcal{E}_1$, and Eq. (7) is written as

$$N(\mathcal{E}) = \frac{n_0\pi\ell}{a}\frac{\mathcal{E}_{\max}-\mathcal{E}}{\mathcal{E}^2}, \tag{8}$$

where ℓ is the distance from the surface to the position where the accelerating electric field, the generated ion energy, of the surface is $1/e$ at $r = 0$ which is the center of the target surface. Figure 7 (line B) shows this theoretical result, and $\ell = 1$ nm, as in line A. The theoretical and simulation results agree well, although in the low-energy range, $\mathcal{E} < 1.5$ MeV/u, the theoretical results are slightly higher than the simulation results.

In Fig. 7, we set ℓ to 1 nm, but in other words, from this result we can say that, under the conditions of our study, those become carbon ions and accelerated by laser irradiation is at a depth of approximately 1 nm from the target surface. Equation (5) indicates that the thickness, $\delta_1(r)$, at which the ions of energy $\mathcal{E}_1$ are generated becomes thicker, i.e., the number of generated ions increases, farther away from the origin. This explains why the boundary of each ion bunch is clear, as shown in Fig. 5.

Differentiating Eq. (8) by $\mathcal{E}$, we obtain $dN(\mathcal{E})/d\mathcal{E} = n_0\pi\ell(1-2\mathcal{E}_{\max}/\mathcal{E})/a\mathcal{E}^2 < 0$. Therefore, the energy spectrum decreases monotonically.

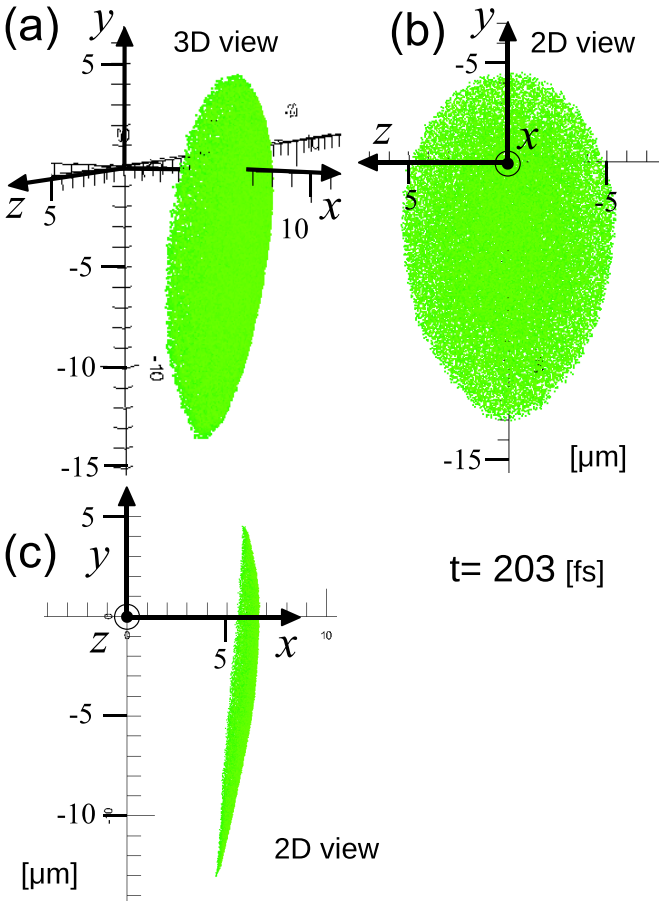

FIG. 8. Spatial distributions of the 4-MeV/u carbon ions at $t = 203$ fs. (a) Three-dimensional view. Two-dimensional views as viewed along the x axis (b) and viewed along the z axis (c).

V. 4-MEV/U CARBON ION BUNCH

In this section, we focus on ions around 4 MeV/u, which is about half of the maximum ion energy, since this energy is required in the application (injectors). The energy range of the ion cloud shall be 10% (4 MeV/u ±5%), i.e., 3.8 – 4.2 MeV/u ions. In the following, unless otherwise noted, "4 MeV/u ion" means to a 3.8–4.2 MeV/u carbon ion traveling in the $+x$ direction. Figure 8 show the spatial distributions of the 4 MeV/u carbon ions at $t = 203$ fs. Figure 8(a) is a 3D view. Figures 8(b) and 8(c) are 2D projections as viewed along the x and z axes, respectively. As shown in Fig. 8(b), the ion cloud has a vertical, y direction, long elliptical distribution, with a slight overall shift in the $-y$ direction. The thickness of the ion cloud is very thin [see Fig. 8(c)] and has a shell-like shape spread along the yz plane. This is because the acceleration process is a Coulomb explosion. In the Coulomb explosion, the ion at the surface of the target becomes the maximum energy ion, and the ion energy decreases as it moves inward from the surface in the direction of the thickness (but only up to half the target thickness). Therefore, an ion at a certain energy, $\mathcal{E}$, occurs only from a certain position, x, in the depth direction. That is, the ions with energy ranging from $\mathcal{E}$ to $\mathcal{E}+\Delta\mathcal{E}$ come from a narrow depth range of x to $x + \Delta x$, so the thickness of its bunch becomes very thin. The ion cloud has a layered structure consisting of shell-like thin ion bunches with different energies, similar to the layers of an onion. Figure 9(a) shows a scatter plot of the 4 MeV/u ions when the horizontal, z direction, and vertical, y direction, velocities are taken on the horizontal and vertical axes, respectively. The ions are long distributed in the horizontal direction, i.e., the ion cloud has a larger horizontal velocity spread than in the vertical direction. In the v_z space [Fig. 9(b)], the number of ions is the largest at $v_z = 0$ (almost at the center of the scatter diagram), and the distribution is symmetric about the $v_z = 0$ axis. Conversely, in the v_y space [Fig. 9(c)], the peak is located at a position that is greatly shifted towards $-v_y$ from the center of the scatter plot, and the distribution is not symmetrical like the v_z space.

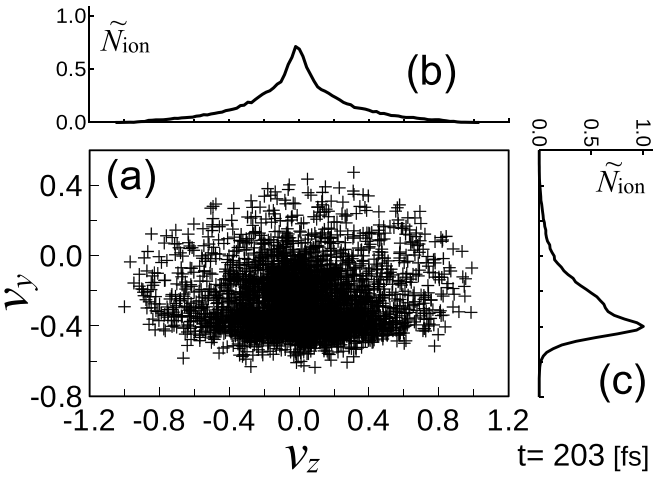

FIG. 9. (a) Scatter plot of the 4-MeV/u ion. The z-direction velocity of carbon ions, v_z, versus y-direction velocity, v_y, normalized by the maximum value of $|v_z|$. (b) Distribution of the number of carbon ions in the v_z space and (c) v_y space. It is normalized by its maximum value in (b) and (c), $\tilde{N}_{\rm ion} = N_{\rm ion}/N_{\rm ion,max}$.

The ion distribution in Fig. 8(b), colored by the velocity of each ion in the y and z directions, is shown in Fig. 10. The darker color indicates that the ion velocity is faster, and the contour levels are the same for (a), (b), and (c). Figure 10(a)

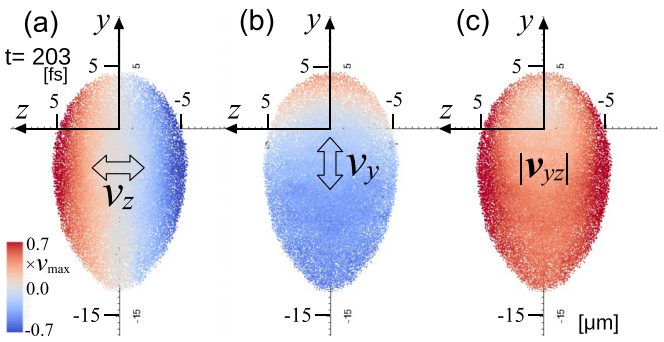

FIG. 10. Ion distribution of Fig. 8(b) colored by the velocity of each ion. Color coded by horizontal velocity v_z (a), by the vertical velocity v_y (b), and by their amplitude $|\boldsymbol{v}_{yz}| = \sqrt{v_z^2 + v_y^2}$ (c) at $t = 203$ fs. Normalized by the maximum v among (a), (b), and (c), i.e., $\max\{|\boldsymbol{v}_{yz}|_i\}$. In the horizontal direction, it expands by about 1.5 times the speed in the vertical direction.

is color coded by the horizontal velocity, v_z, with red representing the velocity in the $+z$ direction and blue in the $-z$ direction. The horizontal velocity is higher toward the two ends of the bunch and is almost zero near its center. That is, in the horizontal direction, the ion bunch expands with its center as the immovable point, and the velocity is faster for the ions at both ends of the horizontal direction. Figure 10(b) is color coded by the vertical velocity, v_y. Overall, the color is lighter than that of Fig. 10(a), i.e., the velocity is lower, and the edges are not noticeably faster. Moreover, the proportion of the blue part is large, indicating that the ion bunch has a downward, $-y$ direction, velocity on average. Therefore, the position that has not moved vertically, i.e., the white area, is shifted in the $+y$ direction from the center of the ion bunch. In Fig. 10(c), the ions are colored by their amplitudes v_z and v_y, $|\boldsymbol{v}_{yz}| = \sqrt{v_z^2 + v_y^2}$. The darkest color (highest velocity) is at both ends of the horizontal direction, and the lightest color (lowest velocity) is located at a position slightly off the $+y$ side from $y = z = 0$. In the horizontal direction, it is expanded by about 1.5 times the speed in the vertical direction. The generated ion bunch has a higher velocity in the horizontal, z, direction than in the vertical, y, direction. That is, thereafter, the ion bunch expands more significantly in the horizontal direction. Consequently, we obtain a 4 MeV/u ion bunch with a large horizontal spread.

Next we explain why the horizontal spread of the velocity vector is greater than that of the vertical vector. In our simulation, we use a 45° obliquely incident laser pulse; thus, the laser irradiating area on the target is a vertically long ellipse centered at $y = z = 0$ [Fig. 2(b)]. Consequently, the acceleration field E_x is distributed over a shorter distance in the horizontal, z, direction than in the vertical, y, direction [Fig. 2(c)]. Thus, E_x changes to a certain value at a short distance in the z direction and changes to that value at a longer distance in the y direction, i.e., $|\partial E_x/\partial z| > |\partial E_x/\partial y|$. The ions are accelerated by E_x; thus, the larger the E_x position, the larger the amount of ion movement in the x direction, δ_x. Therefore, $|\partial \delta_x/\partial z| > |\partial \delta_x/\partial y|$, i.e., the curve of the target surface is steeper in the horizontal, z, direction than in the vertical, y, direction in the early stage of acceleration. This is the reason for the higher velocity in the horizontal direction than in the vertical direction. In our simulation, because of the 45° oblique incidence, the FWHM of the laser intensity in the vertical direction on the target is longer than in the horizontal direction by a factor of $\sqrt{2}$. This can also be expressed as the spot size of the laser in the horizontal direction is smaller than that in the vertical direction. These results demonstrate that the divergence of the ions in the direction of the short spot size is large. This indicates that for two circularly focused laser pulses with different spot sizes, the case with a smaller spot size has a larger divergence of the generated ions than the case with a larger spot size [24]. It was shown that ion beam divergence is also affected by the acceleration time [25].

Generally, in applications, ions generated by laser acceleration are received and used in equipment installed in the latter stage. In this study, we assume that the entrance of the generated ions in the subsequent device is a 10-cm-diameter circular hole located 1.25 m back from the target, i.e., 5 msr in solid angle (Fig. 11). It is assumed that the ions accelerated in the $+x$ direction and within that range are utilized. Therefore, we will examine in detail the characteristics of ions with energy of 4 MeV/u and within a solid angle of 5 msr. Based on the results of the φ distribution in Fig. 3, the circular hole that receives the accelerated ions is placed at an inclination of $-4°$ from the x axis with its face toward the center of the target to receive the largest number of ions (Fig. 11). Figure 12 shows the energy spectrum of carbon ions passing through the circular hole. Here ion passing is defined as the extension of the momentum vector starting from the position of the ion into the circle at $t = 203$ fs. The result for ions at energies greater than 1 MeV/u is shown by a solid line. The spatial distribution of these ions is shown in the inset. The result for all ions accelerated in the $+x$ direction (i.e., the result in Fig. 4) is also shown by a dotted line for comparison. The number of ions passing through the circle is about 40% of the all, except near the maximum energy. Almost all of the ions near the maximum energy pass through the circle due to the inclined arrangement of the circle. For the 4 MeV/u (3.8–4.2 MeV/u) ions, 3×10^8 ions have passed through the circle. That is, 6×10^7 ions are obtained per 1 msr, which is a sufficiently large number for some applications. Although at around the maximum energy, 8 MeV/u, the number of ions with the same energy range, 7.8–8.2 MeV/u, passing it is

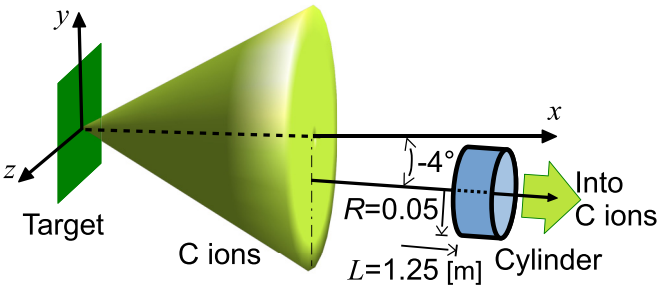

FIG. 11. Illustration of position of the cylinder and the target. The cylinder is placed along a line inclined 4° downward from the x axis, and the center line of the cylinder is on that line.

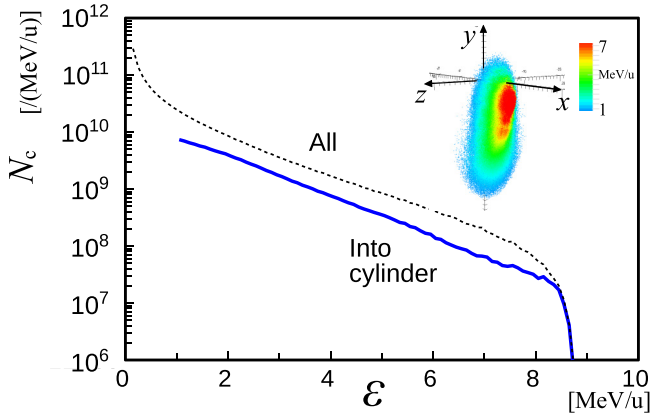

FIG. 12. Energy spectrum of the carbon ions coming into the cylinder in the simulation at $t = 203$ fs is marked by a solid line. Inset: Spatial distribution of those ions. The dotted line is for all ions accelerated in the $+x$ direction.

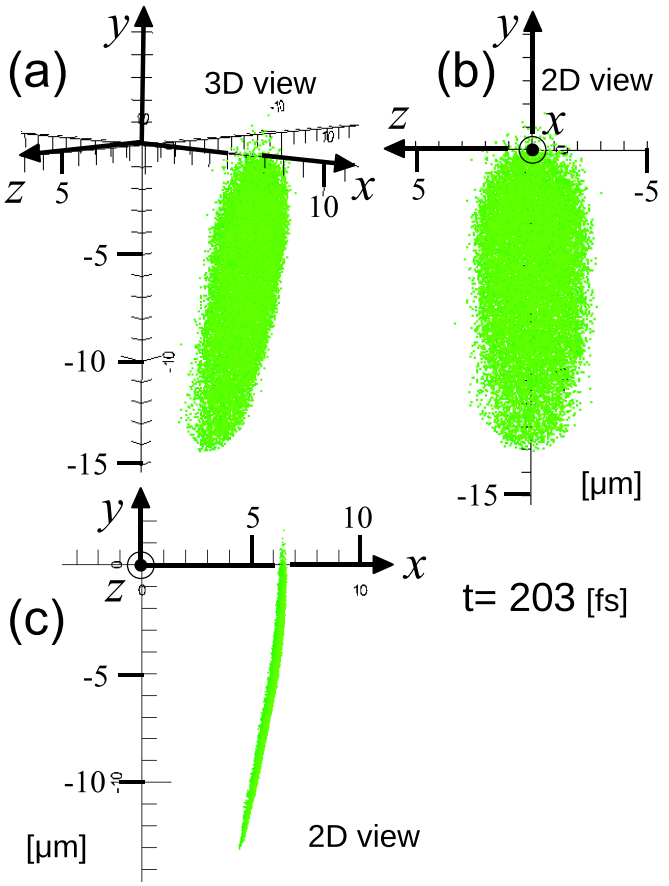

FIG. 13. Spatial distribution of the 4-MeV/u carbon ions at $t = 203$ fs that come into the cylinder. (a) 3D view. The 2D view as viewed along the x axis (b) and along the z axis (c). The ions are distributed vertically elongated.

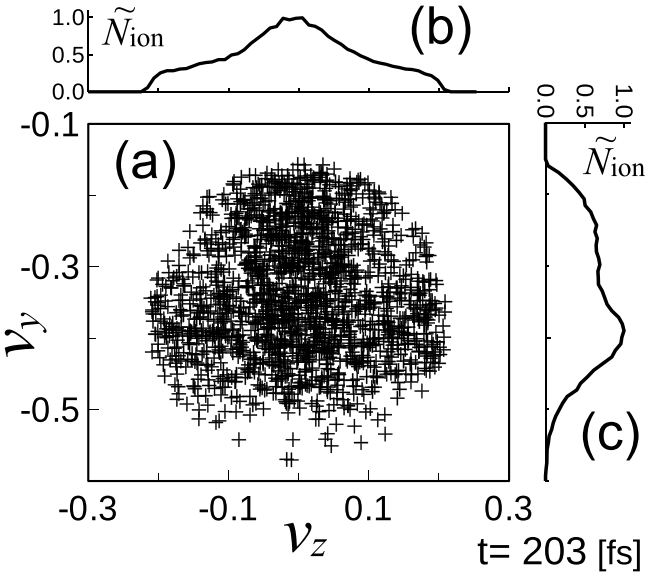

FIG. 14. (a) Scatter plot of the velocities, v_z versus v_y, of the carbon ions shown in Fig. 13, normalized by the maximum $|v_z|$ among all 4 MeV/u ions (i.e., all ions shown in Fig. 8). (b) Distribution of the number of carbon ions in the v_z space, and (c) v_y space. It is normalized by its maximum value in (b) and (c).

2×10^6 /msr, which is significantly less than that at around 4 MeV/u, and is about 1/30. This is the reason for our focus on lower-energy ions, at around 4 MeV/u, instead of near the maximum energy.

Figure 13 show the spatial distributions of the 4-MeV/u carbon ions at $t = 203$ fs that pass through the circle. Figures 13(a), 13(b) and 13(c) correspond to Figs. 8(a), 8(b) and 8(c). That is, Fig. 13(a) shows a 3D view, and Figs. 13(b) and 13(c) are 2D projections as viewed along the x and z axes, respectively. The thickness of the ion bunch is very thin and has a shell-like shape spread along the yz plane. The ion bunch is shifted more toward the $-y$ direction compared to that in Fig. 8 because the circular hole is shifted to $-y$. The distribution of ions is elongated vertically, as shown in Fig. 13(b). The ion distribution through the circle is extremely vertically long because the horizontal, z direction, spread of the velocity vector is larger than the vertical, y direction, spread, as shown in Fig. 10. That is, the ions around the horizontal edges of the ion bunch shown in Fig. 10 do not pass through the circle because of their high horizontal velocity, and the area where the horizontal edges are largely cut off is the ion bunch that passes through the circle. Figure 14(a) presents a scatter plot of v_z versus v_y corresponding to the ions that pass through the circle. It shows a nearly circular distribution, as opposed to the long horizontal distribution in Fig. 9(a). This is because, for the 10-cm-diameter circular hole placed 1.25 m back, this ion bunch is practically almost a point, and the distance from the position of each ion to the edge of the circular hole is approximately the same for all ions. Therefore, the ions passing through the circular hole satisfy the condition $\sqrt{v_y^2 + v_z^2} < r/t$, where r is the radius of the circular hole and t is the time required by the ions to reach the edge of the circular hole, i.e., a circular distribution is formed. In the v_z space [Fig. 14(b)], as shown in Fig. 9(b), it has a peak at $v_z = 0$ and has a symmetrical distribution centered at that position. The difference in the number of ions between the peak and other positions is smaller than that in Fig. 9(b). In the v_y space [Fig. 14(c)], there is also a peak at a position slightly shifted towards $-v_y$, but the peak is not significantly higher than the other positions, as shown in Fig. 9(c), and the overall distribution is relatively flat except at the edge of the scatter diagram.

VI. CONCLUSIONS

Carbon ion acceleration driven by a laser pulse irradiating a carbon foil target is investigated with the help of 3D PIC simulations. In ion acceleration using low-energy laser pulses with solid foil targets, the acceleration process is Coulomb explosion. The ion clouds generated by this scheme have a layered structure with different energies, such as the layers of an onion. An ion bunch extracted with a narrow energy range becomes a thin shell shape with a certain diameter; the higher its energy, the shorter its diameter. The ion energy spectrum monotonically decreases; thus, the lower the energy of the ion, the greater its number. In our simulation, the number of ions generated at around half the maximum energy is

approximately 30 times that near the maximum energy. For applications that require a large number of ions, it is advisable to use ions with lower energy than those with the maximum energy. In the oblique incidence laser, the divergence of the generated ions is smaller in the laser inclination direction than in the direction perpendicular to it. This indicates that the smaller the spot diameter of the laser pulse, the larger the divergence of the ion beam.

The radius of the obtained ion bunch can be expressed in terms of its energy, the maximum generated ion energy, and a coefficient representing the laser intensity distribution. The ion energy spectrum can be expressed by the initial density of the target, and the thickness which becomes accelerated ions in the target, in addition to them. From these formulas, we can obtain important indicators for the design of applications.

ACKNOWLEDGMENTS

I thank S. V. Bulanov, T. Zh. Esirkepov, M. Kando, T. Kawachi, J. Koga, and K. Kondo for their valuable discussions. This work was supported by JST-MIRAI R & D Program Grant No. JPMJMI17A1. The computations were performed with the supercomputer HPE SGI8600 at JAEA Tokai.

[1] S. V. Bulanov, J. J. Wilkens, T. Esirkepov, G. Korn, G. Kraft, S. D. Kraft, M. Molls, and V. S. Khoroshkov, Laser ion acceleration for hadron therapy, Phys.-Usp. **57**, 1149 (2014).

[2] H. Daido, M. Nishiuchi, and A. Pirozhkov, Review of laser-driven ion sources and their applications, Rep. Prog. Phys. **75**, 056401 (2012).

[3] F. Wagner, O. Deppert, C. Brabetz, P. Fiala, A. Kleinschmidt, P. Poth, V. A. Schanz, A. Tebartz, B. Zielbauer, M. Roth, T. Stöhlker, and V. Bagnoud, Maximum Proton Energy Above 85 MeV from the Relativistic Interaction of Laser Pulses with Micrometer Thick CH_2 Targets, Phys. Rev. Lett. **116**, 205002 (2016).

[4] A. Higginson, R. J. Gray, M. King, R. J. Dance, S. D. R. Williamson, N. M. H. Butler, R. Wilson, R. Capdessus, C. Armstrong, J. S. Green, S. J. Hawkes, P. Martin, W. Q. Wei, S. R. Mirfayzi, X. H. Yuan, S. Kar, M. Borghesi, R. J. Clarke, D. Neely, and P. McKenna, Near-100 MeV protons via a laser-driven transparency-enhanced hybrid acceleration scheme, Nat. Commun. **9**, 724 (2018).

[5] J. Badziak, E. Woryna, P. Parys, K. Y. Platonov, S. Jabloński, L. Ryć, A. B. Vankov, and J. Woowski, Fast Proton Generation from Ultrashort Laser Pulse Interaction with Double-Layer Foil Targets, Phys. Rev. Lett. **87**, 215001 (2001).

[6] T. Esirkepov, S. V. Bulanov, K. Nishihara, T. Tajima, F. Pegoraro, V. S. Khoroshkov, K. Mima, H. Daido, Y. Kato, Y. Kitagawa, K. Nagai, and S. Sakabe, Proposed Double-Layer Target for the Generation of High-Quality Laser-Accelerated Ion Beams, Phys. Rev. Lett. **89**, 175003 (2002).

[7] A. P. L. Robinson, A. R. Bell, and R. J. Kingham, Effect of Target Composition on Proton Energy Spectra in Ultraintense Laser-Solid Interactions, Phys. Rev. Lett. **96**, 035005 (2006).

[8] H. Schwoerer, S. Pfotenhauer, O. Jäckel, K.-U. Amthor, B. Liesfeld, W. Ziegler, R. Sauerbrey, K. W. D. Ledingham, and T. Esirkepov, Laser-plasma acceleration of quasi-monoenergetic protons from microstructured targets, Nature (Lond.) **439**, 445 (2006).

[9] T. Toncian, M. Borghesi, J. Fuchs, E. d'Humières, P. Antici, P. Audebert, E. Brambrink, C. A. Cecchetti, A. Pipahl, L. Romagnani, and O. Willi, Ultrafast laser driven micro-lens to focus and energy select MeV protons, Science **312**, 410 (2006).

[10] S. Kar, K. F. Kakolee, B. Qiao, A. Macchi, M. Cerchez, D. Doria, M. Geissler, P. McKenna, D. Neely, J. Osterholz, R. Prasad, K. Quinn, B. Ramakrishna, G. Sarri, O. Willi, X. Y. Yuan, M. Zepf, and M. Borghesi, Ion Acceleration in Multispecies Targets Driven by Intense Laser Radiation Pressure, Phys. Rev. Lett. **109**, 185006 (2012).

[11] T. Morita, T. Z. Esirkepov, S. V. Bulanov, J. Koga, and M. Yamagiwa, Tunable High-Energy Ion Source via Oblique Laser Pulse Incident on a Double-Layer Target, Phys. Rev. Lett. **100**, 145001 (2008).

[12] T. Morita, Laser ion acceleration by using the dynamic motion of a target, Phys. Plasmas **20**, 093107 (2013).

[13] T. Morita, Approach towards quasi-monoenergetic laser ion acceleration with doped target, Phys. Plasmas **21**, 053104 (2014).

[14] H. Kiriyama, A. S. Pirozhkov, M. Nishiuchi, Y. Fukuda, K. Ogura, A. Sagisaka, Y. Miyasaka, M. Mori, H. Sakaki, N. P. Dover, K. Kondo, J. K. Koga, T. Z. Esirkepov, M. Kando, and K. Kondo, High-Contrast High-Intensity Repetitive Petawatt Laser, Opt. Lett. **43**, 2595 (2018).

[15] T. Esirkepov, M. Borghesi, S. V. Bulanov, G. Mourou, and T. Tajima, Highly Efficient Relativistic-Ion Generation in the Laser-Piston Regime, Phys. Rev. Lett. **92**, 175003 (2004).

[16] S. V. Bulanov, E. Y. Echkina, T. Zh. Esirkepov, I. N. Inovenkov, M. Kando, F. Pegoraro, and G. Korn, Unlimited Ion Acceleration by Radiation Pressure, Phys. Rev. Lett. **104**, 135003 (2010).

[17] F. Kroll, F.-E. Brack, C. Bernert, S. Bock, E. Bodenstein, K. Brüchner, T. E. Cowan, L. Gaus, R. Gebhardt, U. Helbig, L. Karsch, T. Kluge, S. Kraft, M. Krause, E. Lessmann, U. Masood, S. Meister, J. Metzkes-Ng, A. Nossula, J. Pawelke *et al.*, Tumour irradiation in mice with a laser-accelerated proton beam, Nat. Phys. **18**, 316 (2022).

[18] K. Noda, Progress of radiotherapy technology with HIMAC, J. Phys.: Conf. Ser. **1154**, 012019 (2019).

[19] C. K. Birdsall and A. B. Langdon, *Plasma Physics via Computer Simulation* (McGraw–Hill, New York, 1985).

[20] T. Morita, Topological investigation of laser ion acceleration, Plasma Phys. Control. Fusion **62**, 105003 (2020).

[21] T. Morita, S. V. Bulanov, T. Z. Esirkepov, J. Koga, and M. Yamagiwa, Control of energy distribution of the proton beam with an oblique incidence of the laser pulse, Phys. Plasmas **16**, 033111 (2009).

[22] K. Zeil, J. Metzkes, T. Kluge, M. Bussmann, T. E. Cowan, S. D. Kraft, R. Sauerbrey, and U. Schramm, Direct observa-

tion of prompt pre-thermal laser ion sheath acceleration, Nat. Commun. **3**, 874 (2012).

[23] S. C. Wilks, A. B. Langdon, T. E. Cowan, M. Roth, M. Singh, S. Hatchett, M. H. Key, D. Pennington, A. MacKinnon, and R. A. Snavely, Energetic proton generation in ultra-intense laser-solid interaction, Phys. Plasmas **8**, 542 (2001).

[24] S. Steinke, J. H. Bin, J. Park, Q. Ji, K. Nakamura, A. J. Gonsalves, S. S. Bulanov, M. Thévenet, C. Toth, J.-L. Vay, C. B. Schroeder, C. G. R. Geddes, E. Esarey, T. Schenkel, and W. P. Leemans, Acceleration of high charge ion beams with achromatic divergence by petawatt laser pulses, Phys. Rev. Accel. Beams **23**, 021302 (2020).

[25] J. S. Green, N. P. Dover, M. Borghesi, C. M. Brenner, F. H. Cameron, D. C. Carroll, P. S. Foster, P. Gallegos, G. Gregori, P. McKenna, C. D. Murphy, Z. Najmudin, C. A. J. Palmer, R. Prasad, L. Romagnani, K. E. Quinn, J. Schreiber, M. J. V. Streeter, S. Ter-Avetisyan, O. Tresca *et al.*, Enhanced proton beam collimation in the ultra-intense short pulse regime, Plasma Phys. Control. Fusion **56**, 084001 (2014).